

Cite this: *RSC Adv.*, 2019, 9, 4445

Microstructure and hydrogen storage kinetics of $\text{Mg}_{89}\text{RE}_{11}$ (RE = Pr, Nd, Sm) binary alloys

Li Chen,^a  Changyi Hu^a and Feng Liu^b

The present work reports the fabrication of $\text{Mg}_{89}\text{RE}_{11}$ (RE = Pr, Sm, Nd) alloys by a vacuum induction furnace. The phase analysis, structure characterization and microstructure observation of $\text{Mg}_{89}\text{RE}_{11}$ alloys were carried out by X-ray diffraction (XRD), scanning electron microscopy (SEM) and transmission electron microscopy (TEM). There exhibits a multiphase microstructure in the as-cast $\text{Mg}_{89}\text{RE}_{11}$ (RE = Pr, Nd, Sm) alloys from the comprehensive analysis made from XRD and SEM, which are containing the major phase ($\text{RE}_5\text{Mg}_{41}$) and several secondary phases (REMg_3 and REMg_{12}). The detections of XRD and TEM reveal that these experimental alloys turn into a MgH_2 nanocrystalline composite with equably distributed RE hydride nanoparticles after hydriding and this MgH_2 major phase turns into a Mg nanocrystalline after dehydriding. The determination results of the hydrogen storage kinetics show that adding the rare earth element (Pr, Sm and Nd) ameliorates the hydriding and dehydriding kinetics of the Mg-based alloys dramatically. The hydrogen desorption activation energy $E_a(\text{de})$ of $\text{Mg}_{89}\text{Pr}_{11}$, $\text{Mg}_{89}\text{Nd}_{11}$, $\text{Mg}_{89}\text{Sm}_{11}$ are 140.595, 139.191, 135.280 $\text{kJ mol}^{-1} \text{H}_2$, respectively. Specially, the hydrogen storage capacity (wt%) of $\text{Mg}_{89}\text{Sm}_{11}$ alloy that added Sm element can reached 5 wt%. The improvement of the hydrogen storage performance of $\text{Mg}_{89}\text{RE}_{11}$ alloys can be principally ascribed to the RE hydride nanoparticles facilitating the hydriding and dehydriding reactions.

Received 30th October 2018
Accepted 28th January 2019

DOI: 10.1039/c8ra08983c

rsc.li/rsc-advances

Introduction

Mg-based alloys have been widely deemed as attractive hydrogen storage materials for hydrogen fuel cells due to their outstanding advantages including good hydrogen storage capacity, low-cost and high accessibility.^{1,2} However, the application of Mg-based alloys has been hampered by their relatively high dehydrogenation temperature and sluggish hydriding/dehydriding kinetics all along.^{3,4} Among the methods to improve the hydriding/dehydriding kinetics, finding effective alloying elements has been one of the most important research focuses for Mg-based alloys.

So far, a variety of chemical elements, such as In,^{5–7} Ni,^{8–10} Zr,^{11,12} Ag,¹³ Al,^{14,15} Ti,^{16,17} rare earth (RE) elements¹⁸ and their composites,^{19–23} have been exploited as the alloying elements for the Mg-based alloys. Among them, adding RE elements attracts extensive interest for the Mg-based alloys due to its excellent improvement of the hydriding/dehydriding rate, which may be a better choice to meet the requirements of future hydrogen energy storage systems.^{24–29} Therefore, the addition of rare earth elements into Mg-based alloys as alloying elements shed light on the better hydrogen storage properties for alloys. The hydrogen storage capacity of $\text{La}_2\text{Mg}_{17}$ reaches 6 wt% at the temperature of

350 °C.³⁰ The Mg_3La compound prepared by induction melting can absorb 2.89 wt% of hydrogen reversibly at 296 °C.³¹ Wu *et al.*³² investigated the hydrogen storage properties and phase transitions of $\text{Mg}_{17}\text{Ba}_2$, which has reversible hydrogen capacity of 4.0 wt% H_2 . Ma *et al.*^{33,34} proposed the addition of Ni to the CaMg_2 -based alloys resulted in room-temperature hydrogen absorption without an activation process, and a maximum hydrogen-absorption capacity of 5.65 wt%. Moreover, dual-tuning effects of the thermodynamics and kinetics for Mg-based materials is one of the key issues for hydrogen economy and hydrogen storage materials.^{35–37} Cao *et al.*³⁵ found that the $\text{Mg}_{85}\text{In}_5\text{Al}_5\text{Ti}_5$ alloy displays both enhanced dehydriding kinetics and thermodynamics, which is prepared by plasma milling (P-milling).³⁶ The addition of In into Mg_2Ni not only greatly enhanced the dehydriding kinetics but also significantly lowered the thermodynamic stability.³⁷

Although the research of Mg-based hydrogen storage alloys has made much substantial progress, the cost of hydrogen storage alloys has been increased by high alloying element content, and the hydrogen storage performance needs to be further improved. In this work, we report a time-saving vacuum inducing smelting method to synthesize low alloying $\text{Mg}_{89}\text{RE}_{11}$ (RE = Pr, Nd, Sm) binary alloys as new hydrogen storage materials. On the one hand, we evaluated hydrogen storage properties of the $\text{Mg}_{89}\text{RE}_{11}$ (RE = Pr, Nd, Sm) binary alloys. On the other hand, we deeply discussed the hydriding and dehydriding mechanism for the $\text{Mg}_{89}\text{RE}_{11}$ (RE = Pr, Nd, Sm) binary alloys further.

^aKunming University of Science and Technology, Kunming 650093, China^bKunming Institute of Precious Metals, Kunming 650106, China. E-mail: 669282531@qq.com

Experimental

The compositions of alloys in this experiment were designed to be $\text{Mg}_{89}\text{RE}_{11}$ (RE = Pr, Nd, Sm). The alloy ingots were melted and synthesized with a certain mass ratio metal by using a vacuum induction furnace. In order to prevent the volatilization and oxidation of magnesium and rare earth elements, 0.04 MPa helium was used as the protection gas in the smelting process. After the liquid alloy is injected into the copper mold, the parent alloy ingot is obtained after cooling.

Some microstructures of the samples, including microscopic morphology, phase composition and crystal structure, were observed and characterized by TEM (JEM-2100F) linked with an SAED (selected area electron diffraction), SEM (FEI Quanta 400) linked with an EDS (Energy Disperse Spectroscopy, EDAX Apollo 40 silicon drift detector). For phase analysis, XRD (D/max/2400) technique was employed.

A series of tests on the kinetics of hydrogen absorption and desorption of alloys were carried out on an automatically controlled Sieverts apparatus. The alloys used in above test need to be mechanically pulverized in advance and the powder between 48–75 μm is screened for testing. The sample weighing 1 g was put into the reaction chamber and repeatedly absorbed/desorbed hydrogen until completely activated. When the initial hydrogen pressure of hydriding process was set at 3 MPa, the hydrogen absorption experiment was carried out in the temperature range of 150–380 $^{\circ}\text{C}$. At the same temperature, the initial hydrogen pressure in hydrogen desorption was set at 1×10^{-4} MPa.

Results and discussion

Microstructure of as-cast $\text{Mg}_{89}\text{RE}_{11}$ (RE = Pr, Nd, Sm) binary alloys

The phase composition and phase structure of the as-cast $\text{Mg}_{89}\text{RE}_{11}$ (RE = Pr, Nd, Sm) binary alloys are shown contrastively in the XRD diagram of Fig. 1. These three alloys have the typical crystalline structure. After the analysis using the Jade 6.0 software on the crystal cell parameters of the phase of as-cast alloys, we could find the as-cast $\text{Mg}_{89}\text{Pr}_{11}$ alloy is composed of major phase $\text{Pr}_5\text{Mg}_{41}$ with space group of $I4m$ tetragonal structure (the lattice parameters are showing $a = b = 1.4780$ nm, $c = 1.0430$ nm) and secondary phase PrMg_3 with space group of $Fm\bar{3}m$ cubic structure (the lattice parameter is showing $a = 0.7388$ nm) and PrMg_{12} with space group of $I4mmm$ tetragonal structure (the lattice parameters are showing $a = b = 1.0340$ nm, $c = 0.5980$ nm). The as-cast $\text{Mg}_{89}\text{Nd}_{11}$ alloy contains major phase $\text{Nd}_5\text{Mg}_{41}$ with space group of $I4m$ tetragonal structure (the lattice parameters are showing $a = b = 1.4760$ nm, $c = 1.0390$ nm) and secondary phase NdMg_3 with space group of $Fm\bar{3}m$ cubic structure (the lattice parameter is showing $a = 0.7438$ nm) and NdMg_{12} with space group of $I4mmm$ tetragonal structure (the lattice parameters are showing $a = b = 1.0310$ nm, $c = 0.5930$ nm). The as-cast $\text{Mg}_{89}\text{Sm}_{11}$ alloy is made up with two parts, major phase $\text{Sm}_5\text{Mg}_{41}$ with space group of $I4m$ tetragonal structure (the lattice parameters are showing $a = b = 1.4815$ nm, $c = 1.0366$ nm) and secondary

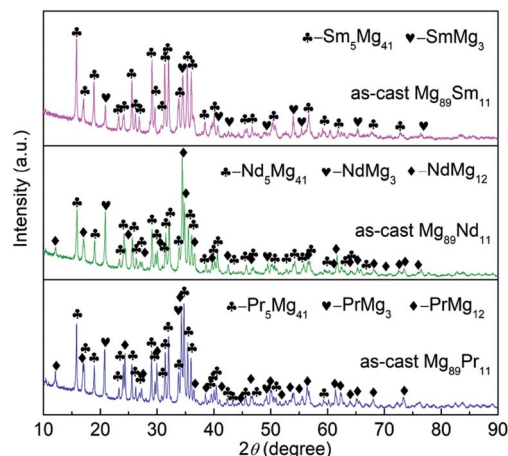


Fig. 1 XRD patterns of as-cast samples for $\text{Mg}_{89}\text{RE}_{11}$ (RE = Pr, Nd, Sm) alloys.

phase SmMg_3 with space group of $Fm\bar{3}m$ cubic structure (the lattice parameter is showing $a = 0.7346$ nm). Unlike the $\text{Mg}_{89}\text{Sm}_{11}$ alloy, both $\text{Mg}_{89}\text{Pr}_{11}$ alloy and $\text{Mg}_{89}\text{Nd}_{11}$ alloy include three different types of phases. The stronger the secondary phase diffraction peaks of $\text{Mg}_{89}\text{Pr}_{11}$ alloy and $\text{Mg}_{89}\text{Nd}_{11}$ alloy express, the higher the secondary phase content will be.

Fig. 2 displays the SEM micrographs of as-cast $\text{Mg}_{89}\text{RE}_{11}$ (RE = Pr, Nd, Sm) binary alloys. Taking as-cast $\text{Mg}_{89}\text{Sm}_{11}$ alloy as an example, the EDS patterns of A and B regions are depicted to represent the alloy content of each region. The two regions with different degrees of darkness in the as-cast alloy represent the two-phase structure of the alloy. The results combining the EDS and XRD analysis show that the white and dark gray areas are SmMg_3 and $\text{Sm}_5\text{Mg}_{41}$, respectively.

Hydriding and dehydriding mechanism

The XRD patterns of the $\text{Mg}_{89}\text{RE}_{11}$ (RE = Pr, Nd, Sm) binary alloys after hydrogen absorption/desorption completely are shown in Fig. 3, all of which alloys display the typical crystalline structure. For $\text{Mg}_{89}\text{Pr}_{11}$ alloy, there are three phases formed after hydrogen absorption, including the major phase MgH_2 with space group of $P4_2/mnm$ tetragonal structure (the lattice parameters are showing $a = b = 0.4517$ nm, $c = 0.3020$ nm) and secondary phase PrH_2 with space group of $Fm\bar{3}m$ cubic structure (the lattice parameter is showing $a = 0.5486$ nm) and $\text{Pr}_8\text{H}_{18.96}$ with space group of $I4_1md$ tetragonal structure (the lattice parameters are showing $a = b = 0.5494$ nm, $c = 1.1078$ nm). While after hydrogen desorption, the major phase Mg with space group of $P6_3/mmc$ hexagonal structure (the lattice parameters are showing $a = b = 0.3209$ nm, $c = 0.1624$ nm) and secondary phase PrH_2 are existing. With respect to $\text{Mg}_{89}\text{Nd}_{11}$, the major phase MgH_2 and secondary phase Nd_2H_5 with space group of $I4_1md$ tetragonal structure (the lattice parameters are showing $a = b = 0.5413$ nm, $c = 1.0870$ nm) exist after hydrogen absorption. And the major phase Mg and secondary phase Nd_2H_5 form after hydrogen desorption. With regard to $\text{Mg}_{89}\text{Sm}_{11}$, the major phase MgH_2 and secondary phase Sm_3H_7 with space



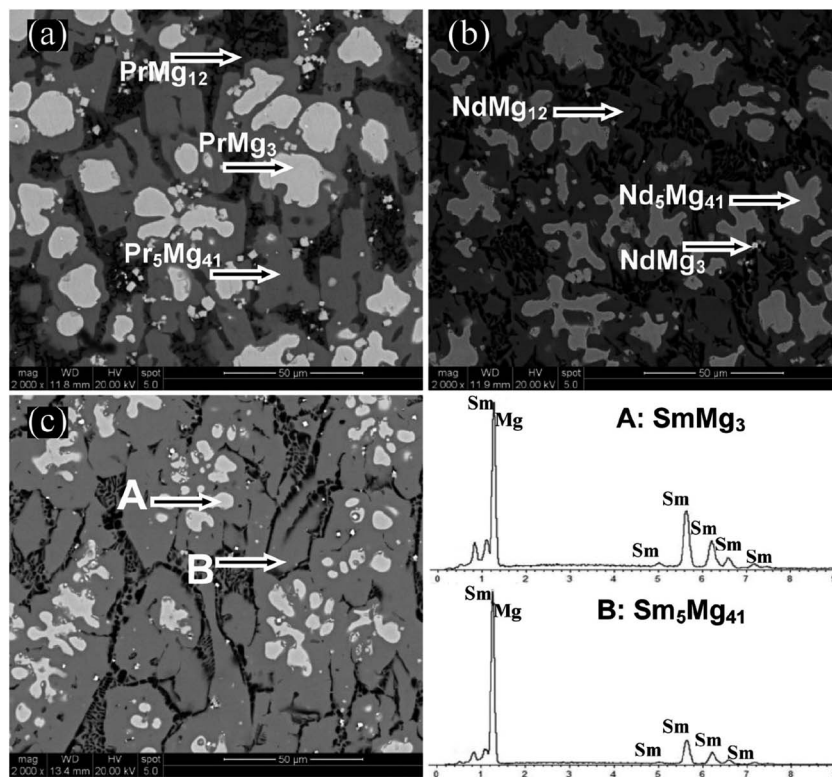


Fig. 2 SEM micrographs and EDS of as-cast samples for $\text{Mg}_{89}\text{RE}_{11}$ (RE = Pr, Nd, Sm) alloys: (a) RE = Pr; (b) RE = Nd; (c) RE = Sm.

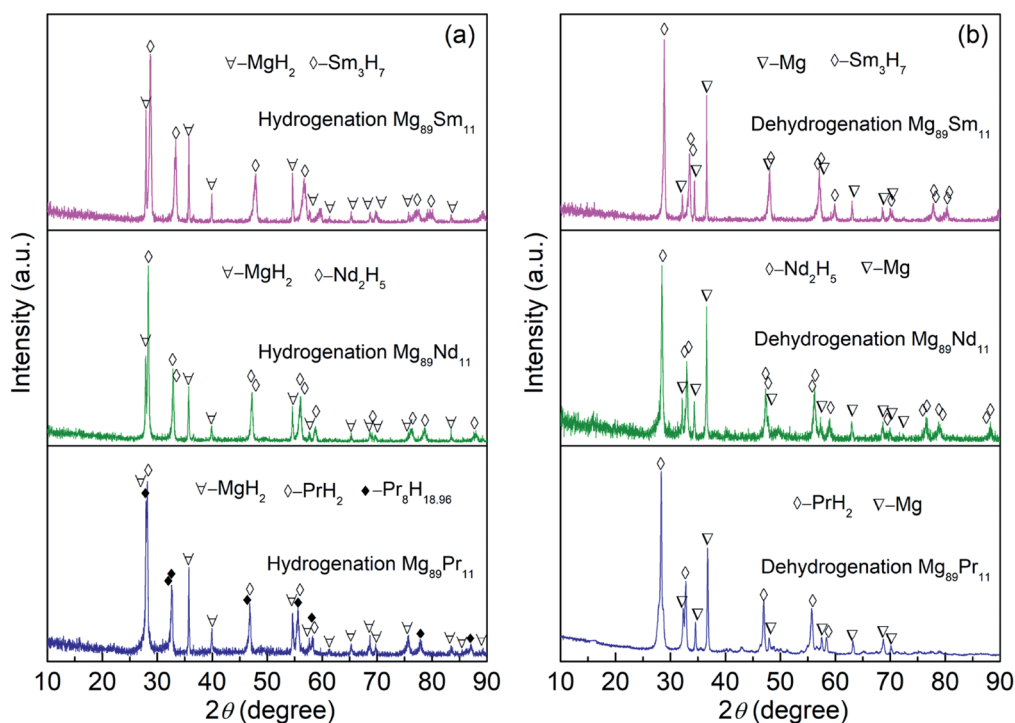


Fig. 3 XRD spectrum of saturated hydrogenation and fully dehydrogenation samples at 380 °C for $\text{Mg}_{89}\text{RE}_{11}$ (RE = Pr, Nd, Sm) alloys: (a) saturated hydrogenation samples; (b) fully dehydrogenation samples.



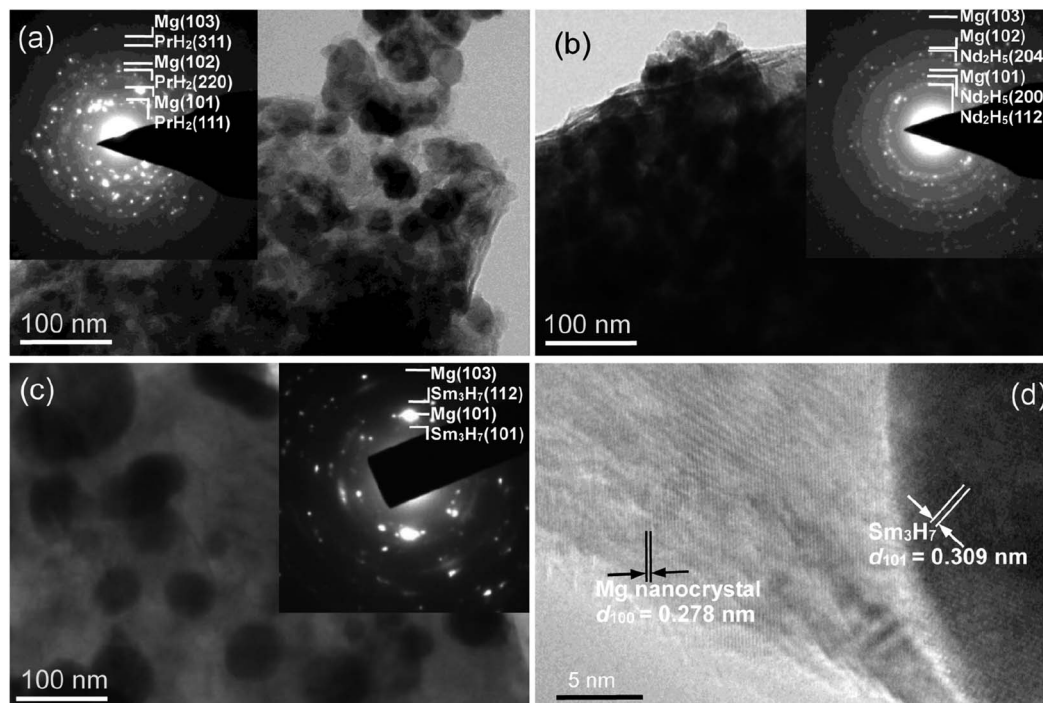


Fig. 4 TEM and HRTEM micrographs and SAED rings of the hydrogen desorption samples for $\text{Mg}_{89}\text{RE}_{11}$ (RE = Pr, Nd, Sm) alloy: (a) RE = Pr; (b) RE = Nd; (c) and (d) RE = Sm.

group of $I4m$ tetragonal structure (the lattice parameters are showing $a = b = 0.3778$ nm, $c = 0.5365$ nm) form after hydrogen absorption. It is the major phase Mg and secondary phase Sm_3H_7 that are existing after hydrogen desorption. It

can be concluded that the hydride PrH_2 , Nd_2H_5 and Sm_3H_7 possess characteristics of good thermal stability at 400°C .³⁸ According to the XRD analysis and literature,³⁸ we infer conceivable reaction pathways:

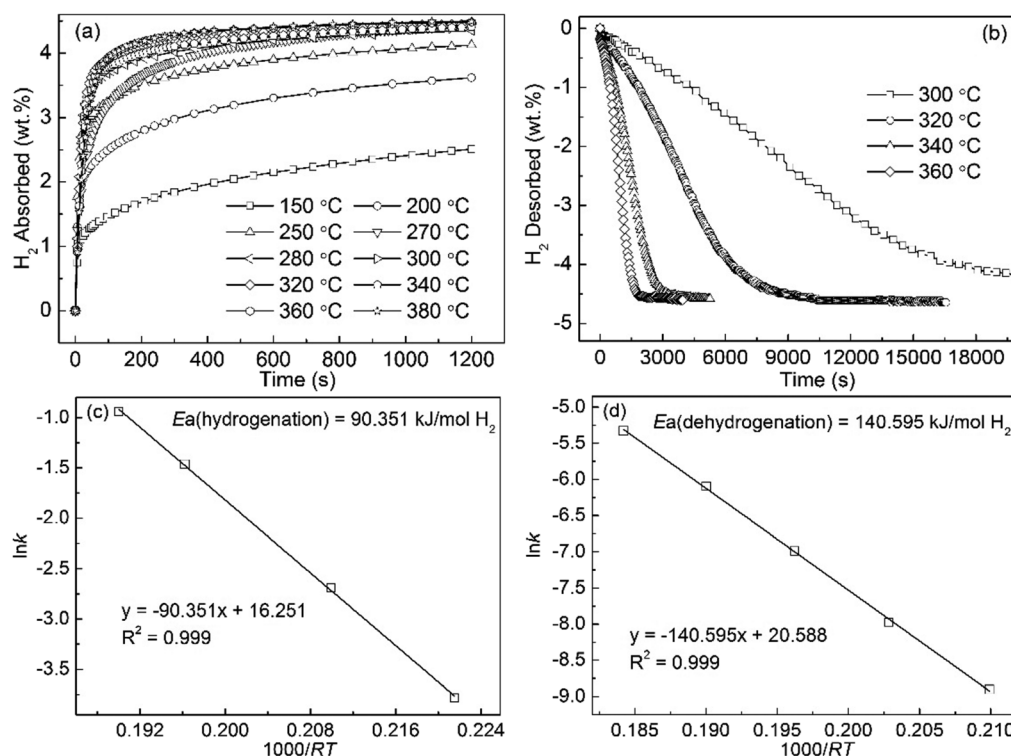


Fig. 5 Isothermal hydrogen absorption (a) and desorption (b) kinetic curves of $\text{Pr}_{11}\text{Mg}_{89}$ alloy at different temperatures and the corresponding Arrhenius plots (c) and (d).



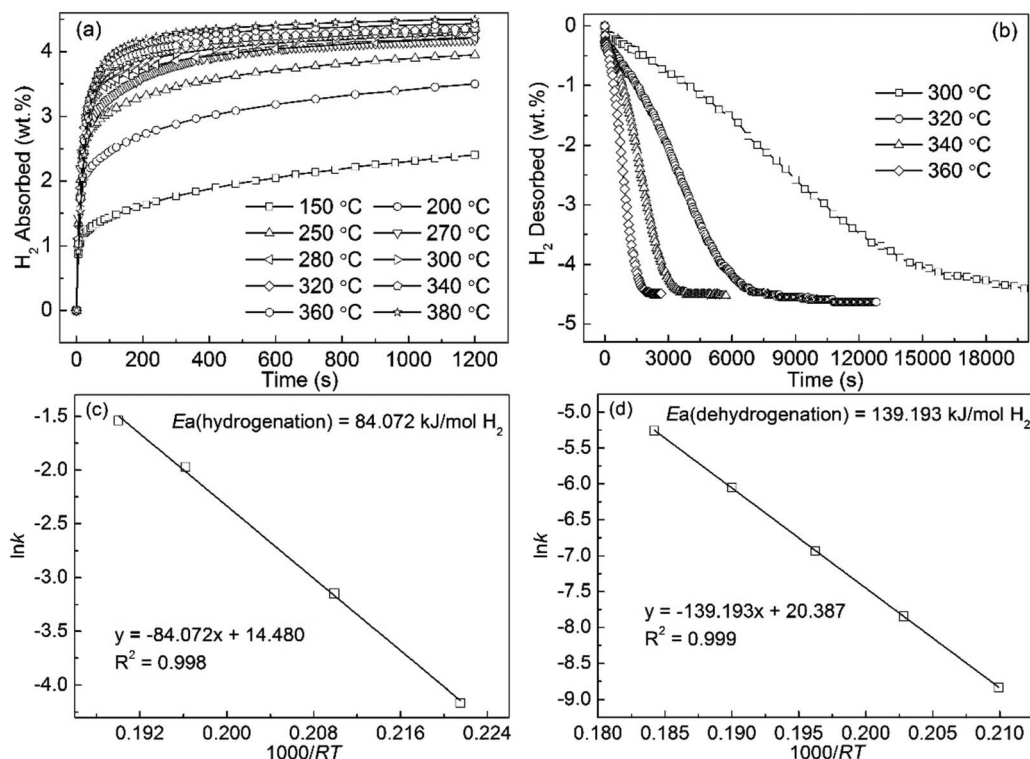
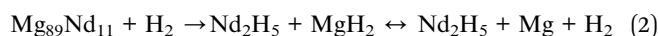
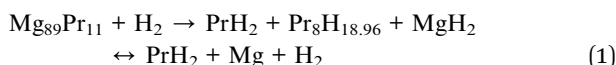


Fig. 6 Isothermal hydrogen absorption (a) and desorption (b) kinetic curves of Nd₁₁Mg₈₉ alloy at different temperatures and the corresponding Arrhenius plots ((c) and (d)).



The fundamental reason for reversible hydrogen absorption/desorption of the active Mg₈₉RE₁₁ (RE = Pr, Nd, Sm) binary alloys is coming from the formation and decomposition of MgH₂.

Fig. 4 shows the TEM and HRTEM micrographs and SAED rings of the fully hydrogen desorption samples at 380 °C for Mg₈₉RE₁₁ (RE = Pr, Nd, Sm) alloy. According to the inset of Fig. 4(a)–(c), the alloys are composed of the Mg and REH_x (PrH₂, Nd₂H₅ and Sm₃H₇) nanocrystal phases, which conforms to the XRD detections. As the observation of the internal lattice structure from HRTEM (Fig. 4(d)), the interplanar spacing of Mg nanocrystalline on (100) crystal surface is 0.278 nm and the secondary phase Sm₃H₇ nanocrystal on (101) crystal surface is 0.309 nm. The hydrogen absorption alloy turns into a Mg nanocrystalline composite with equably distributed Sm₃H₇ nanoparticles (<100 nm) after dehydrogenating. The mechanism of the nucleation and growth of the formed REH_x (PrH₂, Nd₂H₅ and Sm₃H₇) composites is similar to CeH_{2.73}–MgH₂–Ni composites.³⁹ It can be found that the secondary phase PrH₂, Pr₈H_{18.96}, Nd₂H₅ and Sm₃H₇ served as catalysts³⁹ affect the hydrogen absorption and desorption rates.

Hydrogen storage kinetics

For studying the effects of the alloying of Mg with rare earth elements on hydrogen storage kinetics, it is necessary to determine the hydrogen absorption/desorption curves of these Mg₈₉RE₁₁ (RE = Pr, Nd, Sm) binary alloys at various temperatures. The Johnson–Mehl–Avrami–Kolmogorov (JMAK) method can be generally applied to model the hydrogen absorption and desorption data, and there is a linear equation expressed following:⁴⁰

$$\ln[-\ln(1 - \alpha)] = \eta \ln k + \eta \ln t \quad (4)$$

where α , η , k and t are the percentage of Mg converted to MgH₂, the Avrami exponent reaction order, the kinetic parameter and the time, respectively. Based on some experimental data have been measured, we are able to draw the fitting linear plots of $\ln[-\ln(1 - \alpha)]$ vs. $\ln t$ and obtain the η and $\eta \ln k$ values at various temperatures lightly from the slope and intercept of above plots. As a result, the rate constant k will be figured out expediently using eqn (4). Thus, by means of introducing the k values into the following Arrhenius equation, we will calculate the apparent activation energy (E_a) for the absorption and desorption process logically:⁴¹

$$k = A \exp[-E_a/RT] \quad (5)$$

where A , R and T are the temperature independent coefficient, the universal gas constant (8.3145 J K^{−1} mol^{−1}), and the absolute Kelvin temperature, respectively.



Fig. 5(a) shows the hydrogen absorption curves of the $\text{Mg}_{89}\text{Pr}_{11}$ alloy, which were measured at 150 to 380 °C under the initial hydrogen pressure of 3 MPa. The increase of hydrogen absorption capacity will bring with the increase of the temperature for the alloy. It can be suggested that increasing temperature facilitates the improvement of the hydriding kinetics of the alloy. In terms of specific data, the hydrogen absorption capacity of 3.712 wt% for the alloy can be reached within 10 min at 250 °C, compared to only 2.4 wt% for pure MgH_2 even if it lasts 20 min and under the same condition.⁴² Fig. 5(b) displays the hydrogen desorption curves of the $\text{Mg}_{89}\text{Pr}_{11}$ alloy, which were measured at 300 to 360 °C under 1×10^{-4} MPa pressure. The final hydrogen desorption capacity of 4.7 wt% for this alloy is lower than own hydrogen absorption capacity due to the lower final hydrogen pressure ($<1 \times 10^{-2}$ MPa) of the test system. The hydrogen desorption of the hydrogenated alloy at 320 °C, 340 °C and 360 °C have finished within 8235 s, 3420 s and 1890 s, respectively. Unlike no decomposition for the milled MgH_2 at 300 °C, 3.15 wt% H for the $\text{Mg}_{89}\text{Pr}_{11}$ alloy is desorbed in 200 min, suggesting that this alloy displays a good desorption kinetics. Fig. 5(c) and (d) illustrate the Arrhenius plot of $\ln k$ vs. $1000/RT$ under hydrogenation and dehydrogenation conditions, respectively. The calculated activation energy for the hydrogenation ($E_a(\text{ab}) = 90.35 \text{ kJ mol}^{-1}$) is much lower than that of Mg powder after cyclic activation process (100 kJ mol^{-1}).⁴³ For the dehydrogenation, the values of activation energy are 160 and 156 kJ mol^{-1} for un-milled MgH_2 (ref. 44 and 45) and the value of which is $158.5 \text{ kJ mol}^{-1}$ for pure milled MgH_2 ,⁴⁶ which values all show larger than the calculated $E_a(\text{de})$ value ($140.60 \text{ kJ mol}^{-1}$) for the $\text{Mg}_{89}\text{Pr}_{11}$ alloy.

In the initial pressure in the 3 MPa, the hydrogen absorption curves of the $\text{Mg}_{89}\text{Nd}_{11}$ alloy tested at temperatures ranging from 150 to 380 °C are displayed in Fig. 6(a). The hydrogen absorption capacity of the alloy increases from 2.403 wt% at 150 °C to 4.491 wt% at 380 °C. It can be found that the increase of the temperature facilitates the improvement of the hydriding kinetics of the alloy. Under the condition of 250 °C, the hydrogen absorption capacity of 3.712 wt% for the alloy could reach within 10 min. Fig. 6(b) exhibits the hydrogen desorption curves of the $\text{Mg}_{89}\text{Nd}_{11}$ alloy measured at 300 to 360 °C under 1×10^{-4} MPa pressure. The final hydrogen desorption capacity of 4.7 wt% for the alloy is also lower than the hydrogen absorption capacity. The hydrogen desorption of the hydrogenated alloy at 320 °C, 340 °C and 360 °C have finished within 8235 s, 3420 s and 1890 s, respectively. Unlike no decomposition for the milled MgH_2 at 300 °C, 3.45 wt% H for the $\text{Mg}_{89}\text{Nd}_{11}$ alloy is desorbed in 200 min. Fig. 6(c) and (d) illustrate the Arrhenius plot of $\ln k$ vs. $1000/RT$ that is able to reflect the hydrogenation and dehydrogenation kinetics of the $\text{Mg}_{89}\text{Nd}_{11}$ alloy. The calculated $E_a(\text{ab})$ value ($84.072 \text{ kJ mol}^{-1}$) is also much lower than that of Mg powder (100 kJ mol^{-1}). For the dehydrogenation, the $E_a(\text{de})$ value from calculating is $139.193 \text{ kJ mol}^{-1}$ approximately.

The hydrogen absorption curves of the $\text{Mg}_{89}\text{Sm}_{11}$ alloy, which were measured at 150 to 380 °C under 3 MPa hydrogen pressure, shows in Fig. 7(a). The hydrogen absorption capacity of the alloy increases from 2.803 wt% at 150 °C to 5.022 wt% at 380 °C, suggesting that the increasing temperature promotes the improvement of the hydriding kinetics. The hydrogen absorption capacity of 4.112 wt% for the alloy can achieve within 10 min at 250 °C. The hydrogen desorption curves of the

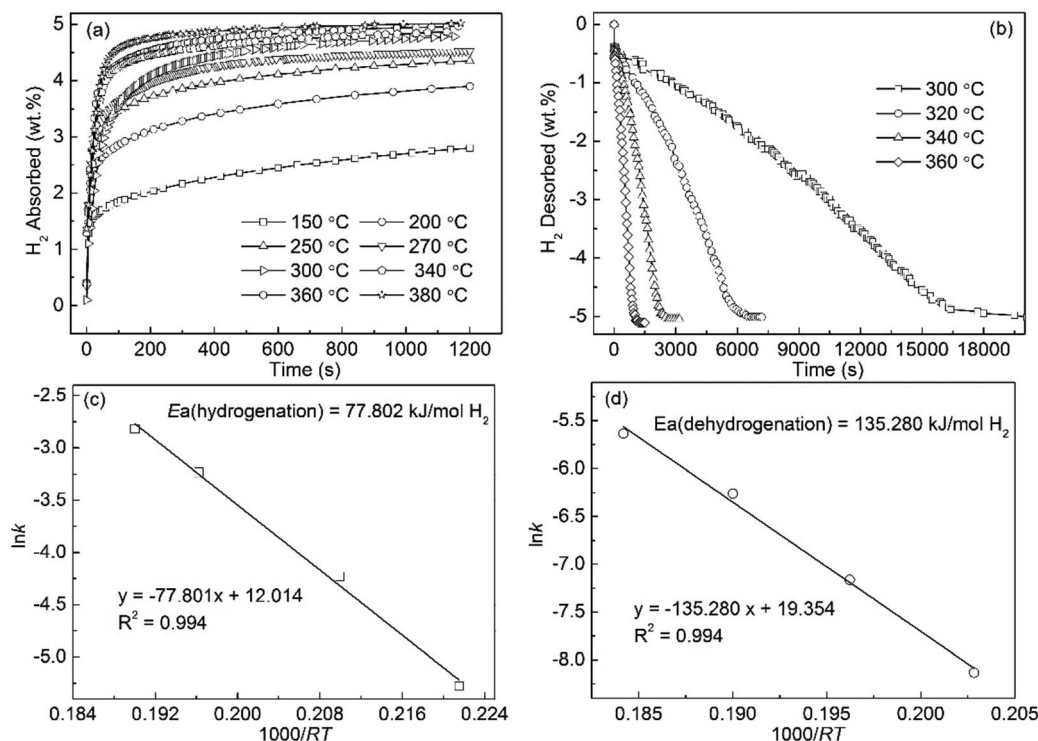


Fig. 7 Isothermal hydrogen absorption (a) and desorption (b) kinetic curves of $\text{Sm}_{11}\text{Mg}_{89}$ alloy at different temperatures and the corresponding Arrhenius plots (c) and (d).

Table 1 Hydrogen storage kinetics properties of Mg₈₉RE₁₁ alloys

Mg ₈₉ RE ₁₁ alloy	250 °C, capacity within 10 min	320 °C, complete dehydrogenation time	<i>E_a</i> (ab) kJ mol ⁻¹	<i>E_a</i> (de) kJ mol ⁻¹
RE = Pr	3.712 wt%	10 350 s	90.35	140.60
RE = Nd	3.895 wt%	8235 s	84.07	139.19
RE = Sm	4.112 wt%	6556 s	77.802	135.28
MgH ₂ (ref. 42–45)	2.4 wt%	Stable	100	156/160

Mg₈₉Sm₁₁ alloy tested at 300 to 360 °C under 1×10^{-4} MPa are depicted in Fig. 7(b). The final hydrogen desorption capacity of 5.0 wt% for the alloy is lower than the hydrogen absorption capacity. Length of time for the completion of hydrogen desorption of the hydrogenated alloy at 320 °C, 340 °C and 360 °C have finished within 6556 s, 2527 s and 1106 s, respectively. Compared to no decomposition for the milled MgH₂ at 300 °C, 3.572 wt% H for the Mg₈₉Sm₁₁ alloy is desorbed in 200 min. The Arrhenius plot of $\ln k$ vs. $1000/RT$ for the hydrogenation and dehydrogenation kinetics are displayed in Fig. 7(c) and (d). The calculated *E_a*(ab) and *E_a*(de) values are about 77.802 kJ mol⁻¹ 135.280 kJ mol⁻¹, respectively.

Synthesizing the above analysis, the hydrogen storage kinetics properties of Mg₈₉RE₁₁ (RE = Pr, Nd, Sm) alloys are listed in the Table 1. For Mg₈₉RE₁₁ (RE = Pr, Nd, Sm) alloys, the order of hydrogen absorption and desorption rate is Sm > Nd > Pr. However, the apparent activation energy (*E_a*) both absorption and desorption course are all decreased, and the order is Sm < Nd < Pr. It can be concluded that the Mg₈₉Sm₁₁ alloy is the highest hydrogen storage kinetics properties alloy. The results shows that the hydrogen sorption properties of Mg-based alloys can be substantially improved by forming composites having catalytic effect and proper microstructure features.^{47–49}

Conclusions

In summary, Mg₈₉RE₁₁ (RE = Pr, Nd, Sm) alloys can be synthesized *via* a time-saving vacuum inducing smelting approach. The conclusions drawn from this work is sketched as blows:

(1) The as-cast Mg₈₉RE₁₁ (RE = Pr, Nd, Sm) alloy contains a major phase RE₅Mg₄₁ (RE = Pr, Nd, Sm) as well as two kinds of secondary phase REMg₃ (RE = Pr, Nd, Sm) or REMg₁₂ (RE = Pr, Nd). After hydrogen absorption, there will form a major phase MgH₂ and a secondary phase PrH₂ and Pr₅H_{18.96} for RE = Pr, Nd₂H₅ for RE = Nd, Sm₃H₇ for RE = Sm. After hydrogen desorption, there will exist the major phase Mg and a secondary phase PrH₂ for RE = Pr, Nd₂H₅ for RE = Nd, Sm₃H₇ for RE = Nd.

(2) The RE hydrides (PrH₂, Nd₂H₅ and Sm₃H₇) are equally distributed in the MgH₂ nanocrystalline phase and possess characteristics of good thermal stability. These RE hydrides (<100 nm) served as catalysts increase the hydrogen absorption and desorption rates. In these three kinds of hydrogen storage alloys, the Mg₈₉Sm₁₁ alloy shows the lowest apparent activation energy both in the absorption and desorption and the fastest hydrogen absorption and desorption rates.

Conflicts of interest

There are no conflicts to declare.

Acknowledgements

This work is financially supported by the National Key R&D Program of China (2016YFB0101309).

References

- 1 K. F. A. Zinsou and J. R. A. Fernández, *Energy Environ. Sci.*, 2010, **3**, 497–676.
- 2 U. D. Rafi, X. Qu and P. Li, *RSC Adv.*, 2012, **2**, 4891–4903.
- 3 N. Juahir, N. S. Mustafa and A. M. Sinin, *RSC Adv.*, 2015, **5**, 60983–60989.
- 4 H. Liu, C. Wu and H. Zhou, *RSC Adv.*, 2015, **5**, 22091–22096.
- 5 Y. S. Lu, M. Zhu, H. Wang, Z. M. Li, L. Z. Ouyang and J. W. Liu, *Int. J. Hydrogen Energy*, 2014, **39**, 14033–14038.
- 6 Z. J. Cao, L. Z. Ouyang, Y. Y. Wu, H. Wang, J. W. Liu, F. Fang, D. L. Sun, Q. G. Zhang and M. Zhu, *J. Alloys Compd.*, 2015, **623**, 354–358.
- 7 L. Z. Ouyang, Z. J. Cao, H. Wang, J. W. Liu, D. L. Sun, Q. A. Zhang and M. Zhu, *J. Alloys Compd.*, 2014, **586**, 113–117.
- 8 S. Løken, J. K. Solberg, J. P. Maehlen, R. V. Denys, M. V. Lototsky and B. P. Tarasov, *J. Alloys Compd.*, 2007, **446–447**, 114–120.
- 9 Y. Wu, M. V. Lototsky, J. K. Solberg, V. A. Yartys, W. Han and S. X. Zhou, *J. Alloys Compd.*, 2009, **477**, 262–266.
- 10 J. L. Bobet, E. Akiba and B. Darriet, *Int. J. Hydrogen Energy*, 2001, **26**, 493–501.
- 11 R. R. Shahi, A. Bhatnagar, S. K. Pandey, V. Shukla, T. P. Yadav, M. A. Shaz and O. N. Srivastava, *Int. J. Hydrogen Energy*, 2015, **40**, 11506–11513.
- 12 B. Molinas, A. A. Ghilarducci, M. Melnichuk, H. L. Corso, H. A. Peretti and F. Agresti, *Int. J. Hydrogen Energy*, 2009, **34**, 4597–4601.
- 13 L. Z. Ouyang, Z. J. Cao, L. Yao, H. Wang, J. W. Liu and M. Zhu, *Int. J. Hydrogen Energy*, 2014, **39**, 13616–13621.
- 14 L. Z. Ouyang, Z. J. Cao, L. L. Li, H. Wang, J. W. Liu, D. Min, Y. W. Chen, F. M. Xiao, R. H. Tang and M. Zhu, *Int. J. Hydrogen Energy*, 2014, **39**, 12765–12772.
- 15 B. P. Mamula, J. G. Novaković, I. Radisavljević, N. Ivanović and N. Novaković, *Int. J. Hydrogen Energy*, 2014, **39**, 5874–5887.
- 16 G. Liang, J. Huot, S. Boily, A. V. Neste and R. Schulz, *J. Alloys Compd.*, 1999, **292**, 247–252.



- 17 Z. Dehouche, J. Goyette, T. K. Bose and R. Schulz, *Int. J. Hydrogen Energy*, 2003, **28**, 983–988.
- 18 S. Kalinichenka, L. Röntzsch, T. Riedl, T. Weißgärber and B. Kieback, *Int. J. Hydrogen Energy*, 2011, **36**, 10808–10815.
- 19 P. Aep, T. Akito and J. S. Szmyd, *Int. J. Hydrogen Energy*, 2009, **34**, 3032–3037.
- 20 H. Y. Leng, Y. B. Pan, Q. Li and K. C. Chou, *Int. J. Hydrogen Energy*, 2014, **39**, 13622–13627.
- 21 S. Hamed, A. Kafrou and A. Simch, *Int. J. Hydrogen Energy*, 2009, **34**, 7724–7730.
- 22 R. Vijay, R. Sundaresan, M. P. Maiya and M. S. Srinivasa, *Int. J. Hydrogen Energy*, 2007, **32**, 2390–2399.
- 23 G. Liang, J. Huot, S. Boily and A. V. Neste, *J. Alloys Compd.*, 2000, **297**, 267–275.
- 24 Z. M. Yuan, T. Yang, W. G. Bu, H. W. Shang, Y. Qi and Y. H. Zhang, *Int. J. Hydrogen Energy*, 2016, **41**, 5994–6003.
- 25 Z. M. Yuan, Y. H. Zhang, T. Yang, W. G. Bu, S. H. Guo and D. L. Zhao, *Renewable Energy*, 2018, **116**, 878–891.
- 26 Z. M. Yuan, W. Zhang, P. L. Zhang, Y. H. Zhang, W. G. Bu, S. H. Guo and D. L. Zhao, *RSC Adv.*, 2017, **7**, 56365–56374.
- 27 Z. M. Yuan, J. He, L. Yang, Z. J. Xia, D. L. Zhao, C. Y. You and W. J. Ren, *J. Appl. Phys.*, 2015, **117**, 17D104.
- 28 Z. M. Yuan, W. Zhang, Y. H. Zhang, S. H. Guo, X. P. Dong and D. L. Zhao, *J. Mater. Sci. Technol.*, 2018, **34**, 1851–1858.
- 29 Y. H. Zhang, Z. M. Yuan, T. Yang, D. C. Feng, Y. Cai and D. L. Zhao, *J. Alloys Compd.*, 2016, **688**, 585–593.
- 30 S. Yajima and H. K. Toma, *J. Less-Common Met.*, 1977, **44**, 301–306.
- 31 L. Z. Ouyang, F. X. Qin and M. Zhu, *Scr. Mater.*, 2006, **55**, 1075–1078.
- 32 D. Wu, L. Ouyang, C. Wu, Q. Gu, H. Wang, J. Liu and M. Zhu, *J. Alloys Compd.*, 2017, **690**, 519–522.
- 33 M. Ma, R. Duan, L. Ouyang, X. Zhu, Z. Chen, C. Peng and M. Zhu, *J. Alloys Compd.*, 2017, **691**, 929–935.
- 34 M. Ma, R. Duan, L. Ouyang, X. Zhu, C. Peng and M. Zhu, *Int. J. Hydrogen Energy*, 2017, **42**, 22312–22317.
- 35 Z. Cao, L. Ouyang, Y. Wu, H. Wang, J. Liu, F. Fang, D. Sun, Q. Zhang and M. Zhu, *J. Alloys Compd.*, 2015, **623**, 354–358.
- 36 L. Ouyang, Z. Cao, H. Wang, R. Hu and M. Zhu, *J. Alloys Compd.*, 2017, **691**, 422–435.
- 37 L. Z. Ouyang, Z. J. Cao, H. Wang, J. W. Liu, D. L. Sun, Q. A. Zhang and M. Zhu, *Int. J. Hydrogen Energy*, 2013, **38**, 8881–8887.
- 38 V. A. Yartys, O. Gutfleisch, V. V. Panasyuk and I. RHarris, *J. Alloys Compd.*, 1997, **253–254**, 128–133.
- 39 L. Z. Ouyang, X. S. Yang, M. Zhu, J. W. Liu, H. W. Dong and D. L. Sun, *J. Phys. Chem. C*, 2014, **118**, 7808–7820.
- 40 T. Sadhasivam, M. S. L. Hudson, S. K. Pandey, A. Bhatnagar, M. K. Singh, K. Gurunathan and O. N. Srivastava, *Int. J. Hydrogen Energy*, 2013, **38**, 7353–7362.
- 41 T. Liu, Y. R. Cao, C. G. Qin, W. S. Chou and X. G. Li, *J. Power Sources*, 2014, **246**, 277–282.
- 42 R. K. Singh, T. Sadhasivam, G. I. Sheeja, P. Singh and O. N. Srivastava, *Int. J. Hydrogen Energy*, 2013, **38**, 6221–6225.
- 43 T. R. Jensen, A. Andreasen, T. Vegge, J. W. Andreasen, K. Ståhl and A. S. Pedersen, *Int. J. Hydrogen Energy*, 2006, **31**, 2052–2062.
- 44 J. Huot, G. Liang, S. Boily, A. V. Neste and R. Schulz, *J. Alloys Compd.*, 1999, **293–295**, 495–500.
- 45 J. F. Fernandez and C. R. Sanchez, *J. Alloys Compd.*, 2002, **340**, 189–199.
- 46 J. F. Mao, Z. P. Guo, X. B. Yu, H. K. Liu, Z. Wu and J. Ni, *Int. J. Hydrogen Energy*, 2010, **35**, 4569–4575.
- 47 M. Zhu, H. Wang, L. Z. Ouyang and M. Q. Zeng, *Int. J. Hydrogen Energy*, 2006, **31**, 251–257.
- 48 J. Cui, H. Wang, J. Liu, L. Ouyang, Q. Zhang, D. Sun, X. Yao and M. Zhu, *J. Mater. Chem. A*, 2013, **1**, 5603–5611.
- 49 Y. Yin, B. Li, Z. Yuan, Y. Qi and Y. Zhang, *RSC Adv.*, 2018, **8**, 34525–34535.

